Grand canonical Monte Carlo study on water agglomerations within a polymer electrolyte membrane fuel cell gas diffusion layer

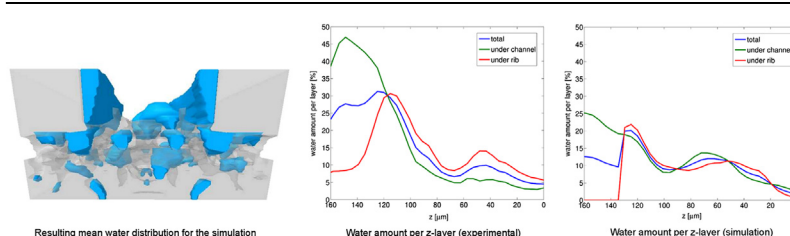K. Seidenberger [a],[*], F. Wilhelm [a], J. Haußmann [a], H. Markötter [b], I. Manke [b], J. Scholta [a]

[a] Zentrum für Sonnenenergie- und Wasserstoff-Forschung Baden-Württemberg, Helmholtzstraße 8, 89081 Ulm, Germany
[b] Helmholtz-Zentrum Berlin für Materialien und Energie GmbH (HZB), Hahn-Meitner-Platz 1, 14109 Berlin, Germany

HIGHLIGHTS

► Development of a grand canonical Monte Carlo model on the μm-scale.
► Simple systems to show the ability of the model to correctly reproduce the properties of water.
► Water distribution within a GDL obtained from synchrotron tomography measurements.
► Mean water distribution of a GDL was analysed performing MC simulations on real GDL structures.
► Comparison of the simulation results to experimental data regarding the inner GDL water distribution.

GRAPHICAL ABSTRACT

Resulting mean water distribution for the simulation

Water amount per z-layer (experimental)

Water amount per z-layer (simulation)

ABSTRACT

Lifetime and durability is one of the most relevant topics regarding PEMFCs. Especially, investigations on water agglomerations within the porous structure of the GDL have become more and more important to completely understand the effects on the fuel cell performance. Besides experimental visualization techniques which help to gain deeper insight the water distribution within the GDL, also different modelling approaches have been developed. We are using and further developing a Monte Carlo model for simulating and analysing the water inventory within PEMFC GDLs taking into account both movements and phase transitions. This model can be employed to identify preferred regions for water agglomerations within the porous structure of the GDL dependent on the surface properties, i.e. the PTFE coverage and the individual structure of the respective material. Our model can use real GDL structures as model input which allows for a direct comparison of the resulting mean water distribution obtained by simulations to experimental results from synchrotron tomography measurements on the same GDL structures. A very good qualitative agreement of the amount of water is found and also preferred regions for water agglomerations are identified consistently for both experiment and simulation.

© 2013 Elsevier B.V. All rights reserved.

1. Introduction

To encounter the challenges related to assuring energy storage and mobility for the future, fuel cells provide a solid perspective on the basis of state-of-the-art technology. Nevertheless, performance, costs and durability are subject of further development, and thereby, the need for *systematic* material development is obvious. Thus reliable models to help understanding the relevant processes and the consequences of changes in both cell and material design are needed.

GDL water management and wettability are critical for achieving optimum fuel cell performance and durability [1]. Fuel cell performance can be affected by water accumulations in the cell,

* Corresponding author.
  E-mail address: katrin.seidenberger@zsw-bw.de (K. Seidenberger).

especially within the cathode GDL, which can reduce the effective distribution of oxygen to the catalytic sites and consequently affect the maximum achievable current density [2]. Furthermore, over the fuel cell lifetime, the GDL hydrophobicity decreases enhancing the formation of such accumulations, thus again a reduction in gas convection and diffusion is induced [1]. The authors of Ref. [1] give a very broad overview of ex-situ and in-situ GDL characterization techniques and also provide a brief insight into some of the simulation methodologies currently used to study PEMFC GDLs. There are plenty well-introduced ex-situ characterization techniques as electrical conductivity measurements, mercury intrusion porosimetry or determination of the gas permeability. Concerning in-situ methods, synchrotron tomography measurements to visualize water within the GDL structure, see e.g. Refs. [3–5], constitute an approved technique. Nevertheless, especially determining the inner-material wetting properties of the porous structure is still challenging, cf. below, and there remains further necessity of combining experimental results into proper models. In this publication, we thus strive to describe recent progress in simulation methodology and results together with the experimental methods which form its basis.

1.1. Wetting properties of the inner GDL surface

Determining the wetting properties of GDL materials is far from being a trivial task; different methods either yield the so-called external contact angle which can be observed on the macroscopic surface of the material or they strive to assign the internal contact angle of the GDL, i.e. to investigate the wetting properties within the porous structure on the micro-scale. The awareness that both are not the same has grown during the last years, several publications have attempted to clarify the subject, e.g. Refs. [6,7], for a recent review of standard methods see Ref. [1]. In short, a droplet lying on the surface of a fibre material as a GDL is not only in contact to solid material as it would be on a smooth surface, but also to air, and furthermore the solid part of a GDL surface is in general far from being homogeneous and smooth. Also the extreme case of droplets adhering to protruding fibres possibly has to be taken into account [8]. The principles governing wettability of simple porous surfaces made of hydrophobic material have been described a long time ago by Cassie and Baxter [9,10], but due to the comparatively complicated properties of common GDL materials, the internal contact angle of the material can only be roughly estimated on the basis of external contact angle data, cf. [11].

External contact angles can be measured employing well-established methods as the sessile drop or the Wilhelmy plate method, cf. [1] and the references therein. The internal contact angle of a porous material to a wetting liquid can be measured by a dynamic sorption experiment according to the Washburn method [12], but as, on purpose, GDLs should be hydrophobic, this rather direct method is not applicable for water. Still one can switch to wetting liquids and, by performing Washburn measurements for several of them having different properties, extrapolate values for the surface energy and contact angle of water, e.g. according to the Owens–Wendt approach [13]. Employing this method, e.g. Gurau et al. [6] and Wood et al. [7] investigated various GDL materials; the internal contact angles reported by these authors range from even slightly hydrophilic values of about 88° (±7) up to approx. 110°. Furthermore, in a recent study Parry et al. [14] employed the Washburn method using water at elevated temperature (66 °C) and found a uniform contact angle of 89° over three different GDL materials, while the Owens–Wendt extrapolation at room temperature yielded very similar values between 90 and 93°. All these values are considerably lower than the 120°–140° [6] or even higher values (see e.g. Ref. [15]) usually found using the sessile drop

method, and considering the fact that the contact angle of pure, smooth PTFE amounts to 108° [13] additionally supports the perception that the sorption measurements result in more reliable values than the methods to determine the external contact angle [1]. Though, provided that the structural properties of the material remain approximatively unchanged, one can still qualitatively assess changes in the wetting properties of the material, cf. for example the study by Chen et al. [15] employing the sessile drop method.

Thus it is clear that the values of the external contact angles are not appropriate as direct input for simulations which aim at describing the behaviour of water within a GDL on the basis of the fundamental properties of the material inner surface. Nevertheless, the combination of Washburn sorption measurements for several liquids and, for example, extrapolation for water following the Owens–Wendt analysis method is known to be quite laborious [1]. Furthermore, Wood et al. were able to show by employing the Wilhelmy method to single fibres extracted from the GDL material that the Owens–Wendt contact angle values for water were found to be between 13° and 19° higher than the single-fibre values for the same material [7]. The authors suspect capillary forces inside the material to be the main reason for this deviation, and they note the dependence of the so-called Washburn or capillary constant on the structural properties of the material, which may lead to variations of this constant by one or two orders of magnitude when dealing with different materials [7], thus making it a very sensitive quantity. For the GDLs considered by Wood et al. for their single-fibre measurements, the contact angles found fell into the range of approximately 80–95° [7]. On one hand, considering the methodology used, these values should be regarded as the most appropriate ones when looking for reliable inner-material properties as simulation input. On the other hand, preparing single fibres from the GDL for sure requires careful proceeding and it may be asked how many fibres are necessary to obtain a representative value for the GDL. Furthermore, it seems unclear to what extend also the preparation might change the surface properties, especially concerning the sites where the fibre used to be in contact to other fibres or to peaces of binder material that can be found in some types of GDLs etc.

Consequently, finding an alternative method to determine the inner-material wetting properties of GDL material while avoiding the difficulties mentioned above involving the influence of the structural and surface properties of the material onto the behaviour towards liquids seems attractive. To investigate general surface properties of material mainly outside the fuel cell research and industry, the inverse gas chromatography (IGC) method has been successfully applied in many studies, see e.g. lit. [16,17]. Being a pure gas-phase method, it can be expected not to be affected by many of the drawbacks of the liquid-based methods mentioned above. Furthermore, employing a very recent device (surface energy analyser (SEA) by Surface Measurements Systems Ltd., London) it is possible to obtain up to monolayer coverage for the adsorption of the probe molecules which allows to measure characteristics representative for the whole surface. In Section 3, a short deduction of the relevant relations based on the theory of van Oss and Good [18] will be given which shows that the components of the surface energy needed to describe wettability and calculate

Table 1
Surface properties of liquids used for surface free energy and contact angle analysis. All values in mJ m^{-2} taken from the liquid database of SMS Ltd, London, UK.

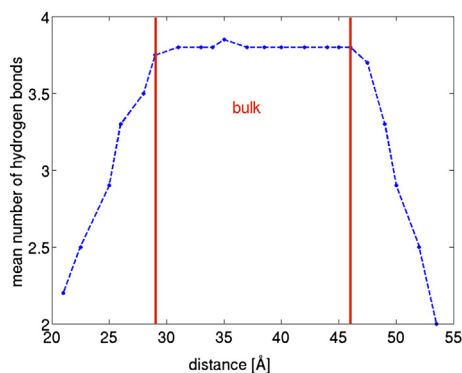| Liquid	γ_{lv}	γ_{lv}^{d}	$\gamma_{lv}^{\oplus}$	$\gamma_{lv}^{\ominus}$
Water	71.98	21.8	25.5	25.5
Dichloromethane			124.58	0.0
Ethyl acetate			0.0	475.67

Fig. 1. Mean number of hydrogen bonds as a function of distance. Sketch was drawn according to data from Ref. [75].

contact angle values to water can be determined from the results of the gas-phase experiment. There has been some discussion in literature concerning the van Oss and Good method, mainly about the liquids to choose and an unambiguous scale of basicity and acidity to be used, for references see Refs. [19,20]. Nevertheless, as long as a self-consistent set of values is used, the value of the contact angle should not be significantly affected by the actual choice of the base scale of basicity and acidity. To the best of our knowledge, so far there has been just one study on GDLs [21] where surface energy values were determined using the IGC technique, but the calculation of contact angle values was not attempted so far.

1.2. Modelling

In recent years, a lot of effort has been put into the development of simulation methods dealing with material and transport properties relevant also for fuel cells. Well known macroscopic models are Computational Fluid Dynamics (CFD) (see Refs. [22,23]), Lattice Boltzmann (LB) [24] or Pore network (PN) models [25]. An application of PN models in the field of fuel cell modelling was presented in Ref. [26]. A pore network model of the gas diffusion layer in a PMFC was developed and validated by Gostick et al. [27].

For further information on nano- and microscopic models one can refer to the authors of Refs. [28–31].The principles of the Monte Carlo (MC) method were first published in Ref. [32] by Metropolis et al. Applications on the atomic or molecular scale can be found e.g. in Refs. [33–36]. Furthermore, the MC method has been extensively used to gain a representation of the structure of porous media and the associated effective properties (for references see Refs. [33–40]).

A very attractive feature of the MC technique is that not only systems containing a fixed number of particles (NVT, canonical ensemble, see e.g. the first version of our model [41,42]) can be described, but also systems featuring variable numbers of particles at constant chemical potential can be tackled (μVT, grand canonical ensemble). This enables the simulation of problems involving ad- and desorption or condensation and evaporation. Recent publications of grand canonical MC models are dealing for example with hydrogen storage in three-dimensional carbon foams using classical grand canonical MC simulations (see Ref. [43]). The
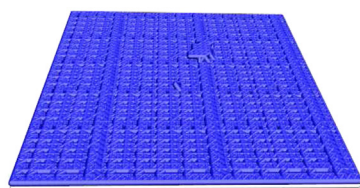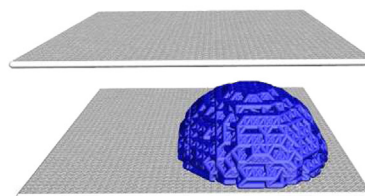

(a) contact angle 10° for the interface liquid / solid.
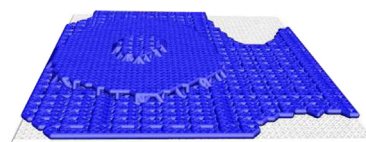
(b) contact angle 45° for the interface liquid / solid.
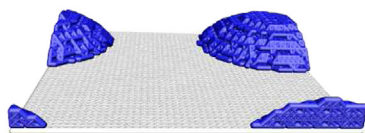
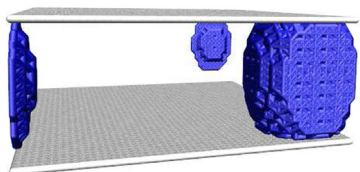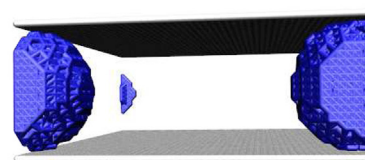(c) contact angle 65° for the interface liquid / solid.

(d) contact angle 85° for the interface liquid / solid.

(e) contact angle 110° for the interface liquid / solid.

(f) contact angle 130° for the interface liquid / solid.

Fig. 2. Mean water distribution on different hydrophilic/hydrophobic smooth surfaces. Note that periodic boundary conditions are applied along the surface plane.
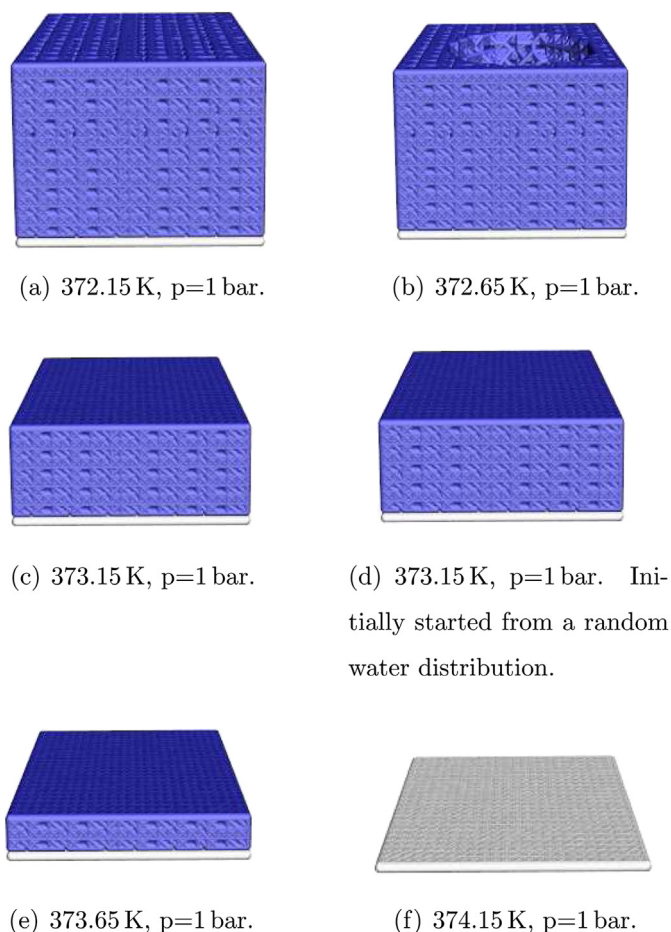
(a) 372.15 K, p=1 bar.

(b) 372.65 K, p=1 bar.

(c) 373.15 K, p=1 bar.

(d) 373.15 K, p=1 bar. Initially started from a random water distribution.

(e) 373.65 K, p=1 bar.

(f) 374.15 K, p=1 bar.

Fig. 3. Grand canonical simulation of a simple system for different boundary conditions. Mean water distribution after reaching a steady state; the system is the same in all cases, in subfigure (a) the complete system is filled.

authors of Ref. [44] are studying surface hydrophilicity-dependent water adsorption on mixed self-assembled monolayers of C_7-CH_3 and C_7-COOH residues.

Molecular models have also been successfully applied to describe transport properties in the membrane or wetting behaviour within the catalytic layer for fuel cell application by Eikerling [45]. Recent publications on fuel cell modelling techniques e.g. can be found in Ref. [46] where 1-D and 2-D two-phase models of polymer electrolyte fuel cells have been developed and employed to investigate through-plane water profiles with spatially-varying properties of GDLs. The results have been compared to experimental data from both neutron radiography and X-ray imaging and showed reasonably good agreement. The authors of Ref. [47] are also presenting a 1-D, two-phase PEMFC model which provides a realistic red description of the physical behaviour of a PEMFC requiring only short simulation times. Liquid water within the cathode gas diffusion layer was considered by using a simplified treatment of the mass balance of water. In Ref. [48], Strahl et al. are presenting a 2-D, non-isothermal, dynamic model of an open cathode for a self-humidified PEMFC to study the effects of water transport/distribution and its influence on the system performance. The authors of Ref. [49] studied the water droplet behaviour in fuel cell channels for different gas channel heights, droplet positions and gas channel wall wettability, using LB simulations. In Ref. [50], the authors are working with a multi-scale method based on a 3D voxel grid. They are able to study an arbitrary distribution of the MPL on and inside the GDL e.g. cracks or different penetration depths. In Ref. [51], the GDL intrusion into gas channels of a PEMFC under different compression values has been investigated using optical measurements, a fluid mechanics model and a finite element analysis (FEM) simulation. The numerical FEM simulation allows for an estimation of the mechanical properties of a GDL by using the measured values of intrusion.

1.3. Synchrotron tomography

Synchrotron X-ray imaging provides a valuable tool for identifying liquid water inside an operating fuel cell. Thus, besides the intrinsic value of its results, it qualifies for validating simulation techniques dealing with liquid water within the cell. For validation of the Monte Carlo method presented herein, synchrotron tomography perfectly suits as it allows for a precise detection of the water distribution in the porous media on the µm-scale delivering 3D information of water accumulations under steady state conditions.

Previous studies concentrated mainly on synchrotron radiography. As shown in Refs. [52,53], high resolution information of the water distribution is available as a cross-sectional view and a through-plane view. In both cases, the cells were designed for small radiation absorption by non-active components. Cells designed for investigations employing a cross sectional view are described in Ref. [54]. But in both viewing directions, only integral information of water accumulations is available, so that a locally resolved water distribution analysis is not possible.

Krüger et al. [3] developed a small fuel cell for tomography measurements which allowed for water detection of very small water clusters down to 4.8 µm/pixel. A further analysis by Markötter et al. [4,5] revealed information about water transport paths through the GDL fibre structure. But a differentiation between liquid water and carbon fibres could not be achieved.

Neutron imaging on the other hand allows for a differentiation of water and carbon materials due to the difference in neutron attenuation [55]. Previous studies proved a good sensitivity for water detection in fuel cells [56,57] and a more detailed analysis with neutron tomography has also been achieved [58]. However, neutron imaging is still inapplicable for detection of single water agglomerations inside the GDL pores because of the limited spatial resolution.

By further development of the synchrotron tomography measurement, the limited water detection ability could be improved. Experimental studies by Eller et al. [59] showed the capability of synchrotron tomography for the differentiation of water and carbon in an operated fuel cell. By subtracting the dry fuel cell images from the images of the operated fuel cell, information of the liquid water distribution can be obtained.

In the present study, this technique is combined with the experience in neutron and synchrotron tomography to develop a feasible measurement setup. Clearly, one issue intrinsically tied to fuel cell tomography experiments is that both the water agglomerations and the cell structure must remain unchanged during image acquisition and furthermore, of course this figuratively frozen state should be representative for the mean water distribution under steady-state fuel cell operating conditions. Both experimental research and recent modelling [60,61] on water transport

Table 2
Results of the IGC experiments for the 25 BC GDL material. All surface energies are given in mJ m^{-2}, DM: dichloromethane, EA: ethyl acetate. Value for DM is set to 0.0 as none of the net retention times for dichloromethane for any surface coverage differed from 0 by a significant value.

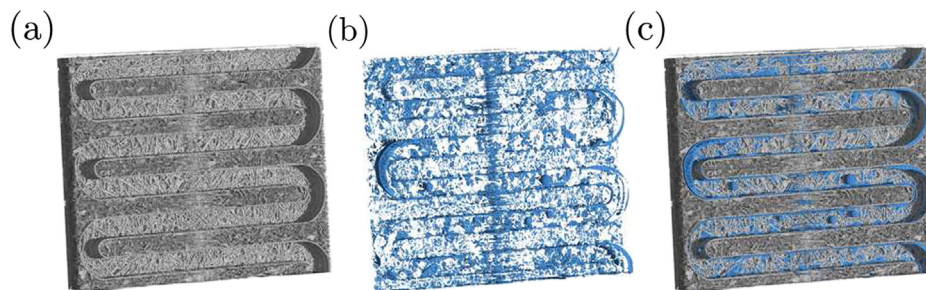| Material	γ_{sv}^d	$\Delta G_{sl}^{a,AB}$(DM)	$\Delta G_{sl}^{a,AB}$(EA)	θ
25 BC	42.9	0.0	35.7	92.0°

Fig. 4. Tomography visualization of the dry fuel cell (a), the water distribution (b) and the combined information (c).

within the cell induced by major temperature gradients show that this is a considerable effect that could be used for water removal during shutdown of the cell. On the other hand, for tomography experiments such an effect during the inevitable shutdown of cell operation before the experiment must be avoided. Using neutron radiography experiments, recently Markötter et al. [62] demonstrated that a shutdown procedure consisting of stopping all flows, closing the gas ports and allowing the cell to cool down to room temperature without active thermal control leaves the cell in a state where the water distribution after 9 h is still practically identical to the moment of shutdown, whereas keeping the ports open and continuing temperature regulation lead to significant changes. In addition, one can assess that the amount of water that will condense from the gas phase within the *sealed* cell is negligible. It is not expected that the general behaviour described above changes with the fuel cell setup or by using synchrotron radiation. Furthermore, the time span needed for acquisition of the synchrotron images is shorter than 2 h. Consequently, employing the shutdown procedure just mentioned, stable quasi in-situ conditions can be assured which are comparable to the steady-state conditions of the model, cf. also Section 5.3.

2. Experimental visualization

2.1. Fuel cell operation

A small fuel cell has been developed for tomographic measurements. It is based on a previous study of Krüger et al. [3]. Mechanical stability and thermal and electrical conductivity have been improved. As membrane electrode assembly the Gore™ Primea® 5761 was chosen and combined with the gas diffusion layer SIGRACET® 25 BC GDL (SGL CARBON GmbH, Meitingen, Germany) on anode and cathode. A single meander design has been chosen as an appropriate flowfield with a channel depth and width of 0.5 mm as well as a land width of 0.5 mm. For the synchrotron measurements, first the fuel cell was operated for 30 min at a cell temperature of 50 °C under constant conditions. Fully humidified gases at a temperature of 50 °C at the cell inlets with a stoichiometry of 2 for hydrogen on the anode and 4 for air on the cathode were provided to run the fuel cell at 1.0 A cm^{-2}. Then gas flows were stopped, gas in- and outlets were closed and the fuel cell was cooled down to ambient temperature to avoid water movements during the tomography.

2.2. Tomographic visualization

The experimental work shown was carried out at the BAMline [63] at the electron storage ring BESSY II of the Helmholtz Centre Berlin in Germany. For the tomographic measurement, the cell was mounted on a rotation table and was stepwise rotated in an angular range of 180° [64]. 1800 projections with a frequency of 3 s were recorded and used for tomographic reconstruction. A 4008 × 2672 pixel CCD detector captured a field of view of 19.2 × 12.8 mm^2 with a pixel size of 4.8 μm. A beam energy of 17 keV was chosen for the experiments [65]. In order to obtain the 3D information of the water distribution, the fuel cell was tomographed in dry and operated state [66]. The datasets of the dry cell and the cell after operation were aligned in terms of rotation and shift in all three dimensions before subtracting the tomogram of the dry cell from the one of the operated cell. The result exclusively consists of the water distribution, which can be further analysed and compared to the water distribution obtained by grand canonical Monte Carlo simulations.

3. Inverse gas chromatography

The IGC method is called *inverse* gas chromatography because here an unknown, porous or fibrous solid material is characterized by its ability to adsorb defined compounds from the gas phase. The method has been in use for over 50 years, current applications comprise e.g. the characterization of pharmaceutical materials [67], for a recent review see lit. [17], polymers [68] and porous materials as silica [69]; for an introductory review cf. lit. [16].

The working principle is to inject a defined amount of solvent vapour into a carrier gas stream of helium. This stream flows through a glass column the sample has been brought to before, so the molecules carried by the flow going through the porous sample can adsorb to its surface. The sample surface is characterized by analysis of the retention times of the probe molecules and the corresponding volumes, which are available by integrating the respective peaks. Thus, inter alia the dispersive and specific components of the surface free energy of the sample can be calculated. Knowing the surface area of the sample from a previous experiment, e.g. a BET measurement, by controlling the amount of solvent vapour injected, the surface coverage can be adjusted. Whereas traditionally, surface energy determination by IGC is performed at infinite dilution, i.e. a very low surface coverage, the so-called finite dilution method has also been in use for several years, see e.g. Ref. [70]. The SEA device used for the measurement reported here is able to conveniently vary the surface coverage from sub-percent to full monolayer coverage if a proper sample size is provided. This avoids the restriction that at low surface coverage, only the highest energy sites can be reached, whereas by investigating the full range of possible surface coverage, expectation values representative for the surface can be calculated.

Table 3
Experimental operating conditions.

T	323.15 K
Relative humidity	≈100%
Current density	1.0 A cm^{-2}

(a) dry tomography data

(b) combined wet and dry tomography data

Fig. 7. Three-dimensional representation of the tomography data with and without water. The extract shown here is the same as in Fig. 8.

$$\Delta G_{sl}^{a} = -\gamma_{lv}(1 + \cos\theta). \tag{2}$$

According to van Oss and Good [18], the free energy of adhesion can be divided into an apolar and a polar component; we note that the original authors use the notation Lifshitz–van der Walls (LW) for the apolar and acid–base (AB) for the polar component.

$$\Delta G_{sl}^{a} = \Delta G_{sl}^{a,LW} + \Delta G^{a,AB}.$$

In a later communication [71], Good in contrast adopts a definition where the interactions due to permanent dipoles are assigned to the LW component. The IGC results presented in the present communication are based on the determination of the dispersive component of the surface free energy γ^d using n-alkanes following the method of Dorris and Gray [72]. This method only involves molecules that do not feature permanent dipoles, the
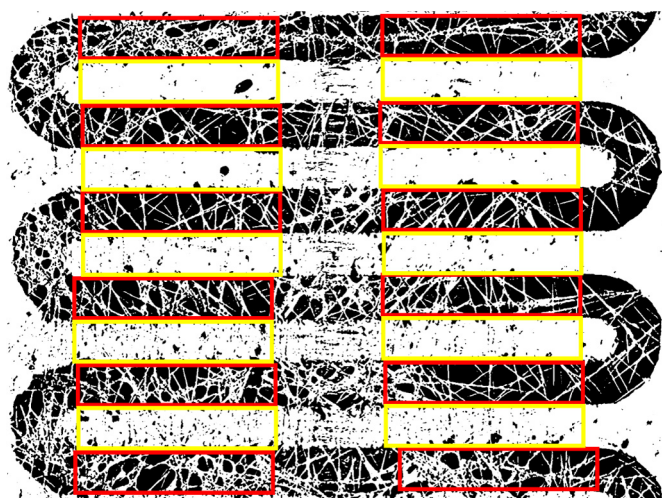

Fig. 5. Regions chosen for calculating the average water amount per layer for the channel area (red) and the land area (yellow). (For interpretation of the references to colour in this figure legend, the reader is referred to the web version of this article.)

3.1. Contact angle determination

In the following section, a mathematical model to calculate the contact angle of water to a solid based on results obtained from IGC measurements and established data of some liquids will be sketched. The results obtained from the IGC measurements are the dispersive component of the surface free energy, γ^d, and the specific component of the free energy of adhesion, $\Delta G^{a,AB}$, AB for acid–base interactions, cf. below.

We start by noting the famous Young equation, which gives the relation between the solid–vapour γ_{sv}, solid–liquid γ_{sl} and liquid–vapour γ_{lv} surface free energy and the liquid–solid contact angle θ

$$\gamma_{sv} = \gamma_{sl} + \gamma_{lv}\cos\theta. \tag{1}$$

Combining this equation and the definition of the free energy of adhesion

$$\Delta G_{sl}^{a} = \gamma_{sl} - \gamma_{sv} - \gamma_{lv}$$
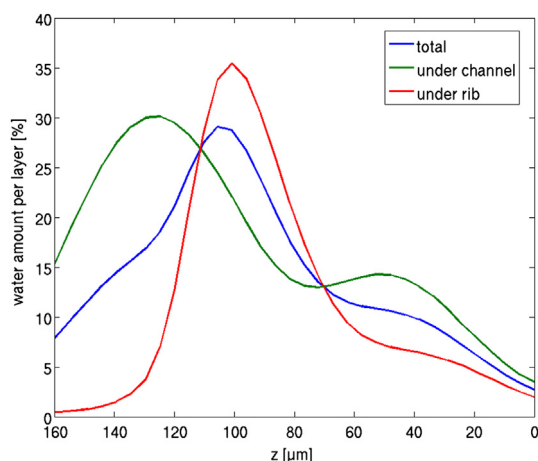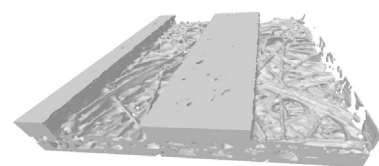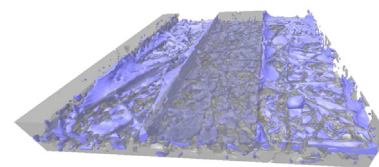
one obtains the Young-Dupré-equation

Fig. 6. Experimental data for the water amount per z-layer. The curves represent mean values for the complete area under consideration, cf. Fig. 5.

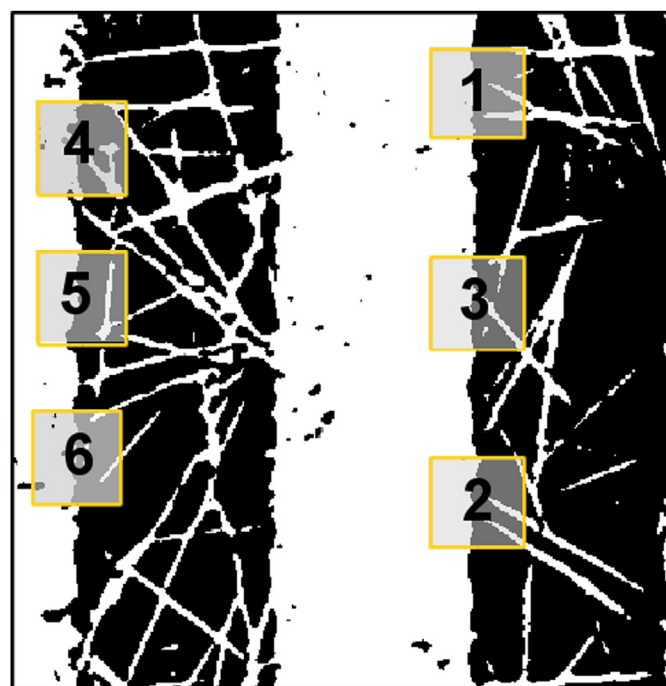**Fig. 8.** Top view of the cell extract used for the MC simulations. The size of this extract is around $1800 \times 1845\ \mu m^2$. Within this region 6 cutouts with a size of $240 \times 240\ \mu m^2$ were defined, all of them containing channel and rib regions half-and-half.

(a) cutout 1

(b) cutout 2

(c) cutout 3

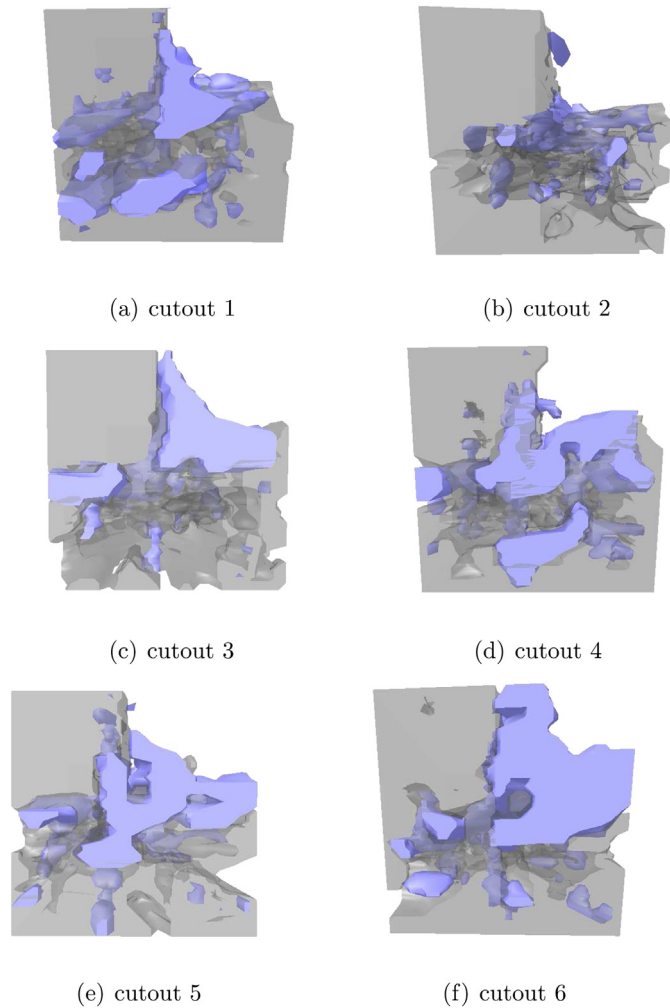(d) cutout 4

(e) cutout 5

(f) cutout 6

Fig. 9. Three-dimensional representation of cutouts 1–6 including the experimental water distribution from synchrotron tomography data.

polarisation approach of Dong et al. [73] used to determine $\Delta G^{a,AB}_{sl}$ for polar liquids yields the difference to γ^d. Consequently, the values should be consistent to the partition according to the van Oss and Good definition, independent of the discrepancies mentioned. To avoid confusion, the more common term dispersive (d) shall be employed in the following instead of Lifshitz–van der Walls (LW).

Applying acid–base theory, the specific component of the free energy of adhesion can be expressed as a function of the acidic $\gamma^{\oplus}$ and basic $\gamma^{\ominus}$ components of the surface free energy of the solid and liquid [18]

$$\Delta G^{a,AB}_{sl} = -2\left(\sqrt{\gamma^{\oplus}_{sv}\gamma^{\ominus}_{lv}} + \sqrt{\gamma^{\ominus}_{sv}\gamma^{\oplus}_{lv}}\right). \tag{3}$$

Taking into account Eq. (2), we arrive at

$$\gamma_{lv}(1 + \cos\theta) = 2\left(\sqrt{\gamma^d_{sv}\gamma^d_{lv}} + \sqrt{\gamma^{\oplus}_{sv}\gamma^{\ominus}_{lv}} + \sqrt{\gamma^{\ominus}_{sv}\gamma^{\oplus}_{lv}}\right). \tag{4}$$

Thus, apart from data on water (see Table 1) known from literature, only the solid–vapour components of the surface free energy have to be known to calculate the contact angle θ. As mentioned above, the dispersive component γ^d_{sv} can be readily taken from the Dorris and Gray analysis of the IGC measurements involving n-alkanes. Determining the acid–base components $\gamma^{\oplus}_{sv}$ and $\gamma^{\ominus}_{sv}$

can be achieved conveniently by choosing appropriate monopolar liquids and performing IGC measurements followed by a polarisation analysis. In the case of monopolar liquids, either the acidic or the polar surface energy component are approximately zero, respectively, so Eq. (3) can be simplified as

$$\gamma^{\ominus}_{sv} = \frac{\left(\Delta G^{a,AB}_{sl}\right)^2}{4\gamma^{\oplus}_{lv}} \quad \text{or} \tag{5}$$

$$\gamma^{\oplus}_{sv} = \frac{\left(\Delta G^{a,AB}_{sl}\right)^2}{4\gamma^{\ominus}_{lv}} \tag{6}$$

and the missing component can be easily calculated on the basis of the respective specific surface energy value obtained from experiment. For the study presented here, dichloromethane ($\gamma^{\ominus}_{lv} \approx 0$) and ethyl acetate ($\gamma^{\oplus}_{lv} \approx 0$) were employed.

3.2. Inner contact angle of the GDL – experimental

The inner contact angle was determined using a device working according to the IGC principle, the surface energy analyser (SEA), Surface Measurement Systems Ltd., London, UK. An approx. 3 mm stripe of a SIGRACET® 25 BC GDL (SGL CARBON GmbH, Meitingen, Germany) weighting approx. 30 mg was brought to a glass column of 4 mm width and 300 mm length. To ensure a clean and dry surface, the column was conditioned for 2 h at 30 °C under a permanent 10 sccm flow of dry helium. Thereupon, the experiments were conducted at 25 °C, 0% RH and at 10 sccm flow rate. To determine the dispersive part of the free surface energy, four n-alkanes (hexane, heptane, octane, nonane) were injected as sketched above. To analyse the specific part, five polar solvents were injected (ethanol, dichloromethane, acetone, ethyl acetate, acetonitrile); as explained before, only dichloromethane and ethyl acetate were actually used to determine the surface free energy components and the contact angle to water. The injections were preformed at 12 target surface coverage values between 2% and 100% monolayer coverage to provide expectation values representative for the surface ($\gamma50$, $dG50$). All liquids were HPLC grade or the best analytical grade available from Sigma–Aldrich Chemie GmbH, Taufkirchen, Germany. The net retention times were calculated taking methane injections as reference. The device operation was controlled by the CIRRUS SEA control software version 1.2.0. The dispersive component of the surface free energy was calculated employing the method introduced by Dorris and Gray [72], the specific free energies of adhesion were determined using the polarisation approach of Dong et al. [73], both methods as implemented in the CIRRUS PLUS analysis software version 1.1.0.

Table 4
Simulation parameters: external conditions and GDL properties.

	Study 1	Study 2
T_{RL}	323.15 K	323.15 K
ΔT_z	–	–
p_{RL}	121.9 hPa	121.9 hPa
Δp_x	–	–
Δp_z	–	–
Humidity (rl)	99%	99%
Humidity (ch)	99%	99%
$\theta_{water/graphite}$	55°	55°
$\theta_{water/GDLmaterial1}$	100°	–
$\theta_{water/GDLmaterial2}$	55°	–
$\theta_{water/GDLmaterial}$	–	92°

(a) cutout 1, contact angle distribution

(b) cutout 1, uniform contact angle

(c) cutout 5, contact angle distribution
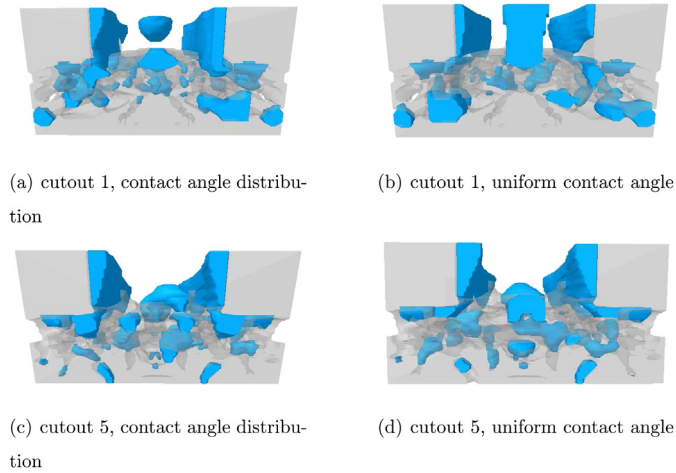
(d) cutout 5, uniform contact angle

Fig. 10. Resulting mean water distribution from the MC simulations for two different cutouts for both GDL material featuring a contact angle distribution and a uniform contact angle.

Further analysis was performed according to the formula given in Section 3.1, the liquid properties used are listed in Table 1.

4. Canonical Monte Carlo model

Within a canonical Monte Carlo model the number of particles, the temperature and the volume are constant (NVT-ensemble) [74]. The acceptance probability for trial moves is given by the following equation:

$$a_{if} = \min\left\{1, \exp\left(-\beta\left(E_f - E_i\right)\right)\right\} \tag{7}$$

where β is defined as:

$$\beta = \frac{1}{k_B T} \tag{8}$$

On the molecular/atomic scale, the interactions between the particles are often described as pair interactions. In contrast, we use surface energy values to calculate particle interactions, because our model is working on the μm scale. The energies in Eq. (7) are energies per molecule/atom. A surface energy value is a specific

Fig. 11. Water amount per z-layer for the experimental data. Mean value for the six regions used for the MC calculations.

quantity. Thus, the amount of water affected by the surface energy is needed. For this reason, we employed a temperature-independent constant β_1 which only considers the relevant water molecules N_S within the surface (S for surface).

Raymond et al. [75] investigated the behaviour of bulk and surface water molecules by means of MD simulations. By analysing the number of hydrogen bonds per water molecule and their strength, they show that the number of H-bonds decreases for water molecules in the surface region. Thus, one can assess the number of water molecules which contribute to the surface energy taking the number of hydrogen bonds as criterion. Within the bulk region, the number of hydrogen bonds has a constant value of around 3.7 hydrogen bonds per molecule and reaches a value of 2 at the surface water/air. At the same time, the bond strength increases. The mean number of hydrogen bonds per molecule as a function of the distance is illustrated in Fig. 1. The number of hydrogen bonds per molecule was calculated as follows: for every oxygen atom all hydrogen atoms within a radius of 2.5 Å were counted.

To assess the volume of the interface region, we assume that the latter starts where the number of hydrogen bonds begins to decrease. Consequently, a value of ≈ 7.5 Å can be estimated according to Fig. 1. Taking into account further theoretical studies from literature, the thickness of this area depends on the MD model used and varies between 3 and 8 Å [76]. Experimental data given by the authors of Ref. [77] yield values between 7 and 18 Å for temperatures between room temperature and 350 K.

Furthermore, the authors of Ref. [76] point out that the water density also decreases near surface. The density averages to a value of around 90% of the bulk value when reaching the surface area.

Thus, based on the results of lit. [75–77], we are able to appraise the volume and accordingly the number of molecules which contribute to the surface energies used within the MC model.

For our MC model, we finally assume that the thickness of layer of molecules contributing to the surface properties has a value of $d = 6.75$ Å. The water density is $\rho_{H_2O} = 0.9982$ kg dm^{-3} (for reference see e.g. Ref. [78]) for the bulk region. As just mentioned, near the surface the density decreases and the value we assume is: $\rho_{H_2O,S} \approx 0.9 \cdot 0.9982$ kg dm$^{-3} = 898.4$ kg m^{-3}.

Thus, for a voxel size of $5 \times 5 \times 5$ μm^3 we can define the interaction volume V_S for a voxel side as follows:

$$V_S \approx 5 \times 10^{-6} \cdot 5 \times 10^{-6} \cdot 6.75 \times 10^{-10} \text{m}^3 = 1.69 \times 10^{-20} \text{m}^3 \tag{9}$$

The mass corresponding to this volume m_S is:

$$m_S \approx \rho_{H_2O,S} \cdot V_S = 1.52 \times 10^{-17} \text{ kg} \tag{10}$$

Taking into account the molar mass of water $M_{H_2O} = 18$ g mol$^{-1} = 0.018$ kg mol^{-1}, we can calculate the number of water molecules which take part in the surface interaction:

$$n_S = \frac{m_S}{M_{H_2O}} = 8.42 \times 10^{-16} \text{ mol} \tag{11}$$

$$N_S = N_A \cdot n_S = 5.07 \times 10^8 \tag{12}$$

So finally, we obtain:

$$\beta_1 = \frac{1}{N_S k_B} = 1.4 \times 10^{14} \text{ K J}^{-1} \tag{13}$$

With β_1 we have deduced a constant considering the relevant number of water molecules per voxel side which are necessary to calculate the acceptance probability for trial moves
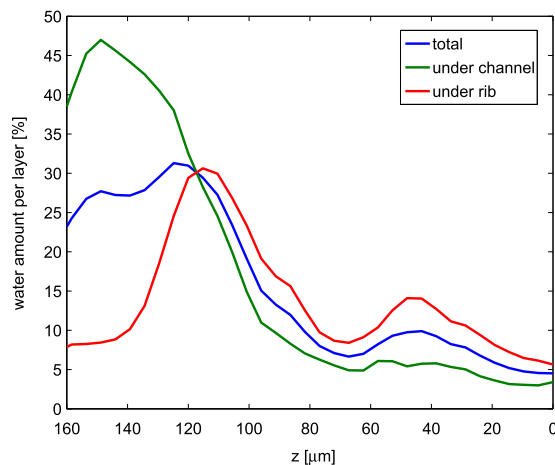
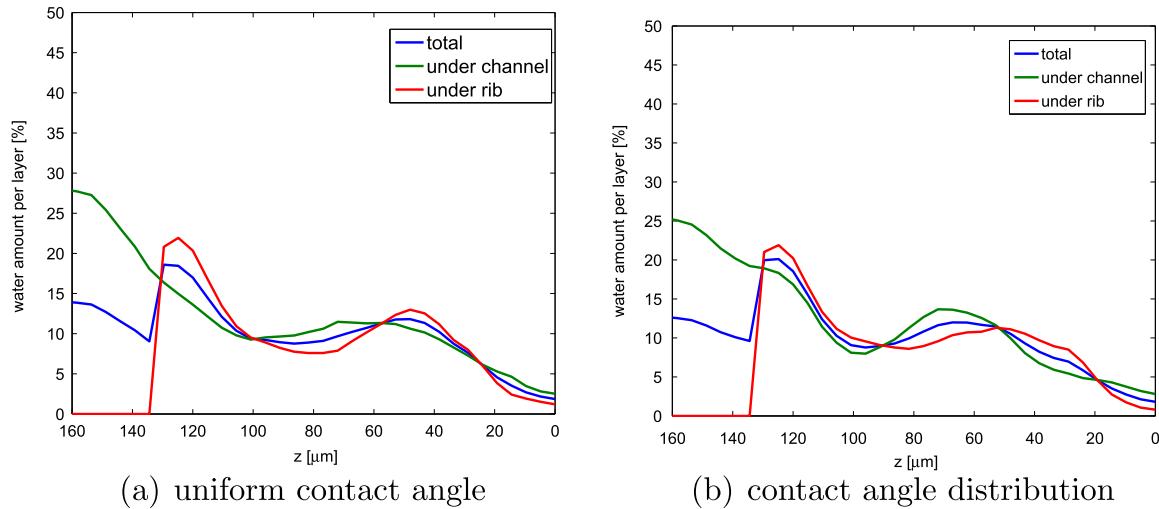(a) uniform contact angle   (b) contact angle distribution

Fig. 12. Water amount per z-layer for the simulation data. Mean value for all six regions used for the MC calculations.

correctly. It is now possible to use real surface energy values from IGC as input parameters for the MC model. The improved canonical MC model now considers all relevant surface energies γ_{sv}, γ_{sl} and γ_{lv} which allows for directly simulating different contact angles according to the Young equation ([71], see also Section 3).

5. Grand canonical Monte Carlo model

Whereas the canonical ensemble features a constant number of particles, volume and temperature, within the grand canonical ensemble the chemical potential, volume and temperature are preset as constant values (μVT-ensemble). For simulating the water distribution within a fuel cell GDL, the μVT-ensemble proves beneficial. This ensemble enables a more realistic description of the water distribution within the GDL, as condensation and evaporation can be additionally taken into account. In an operating PEMFC, water is generated within the reaction layer and then transported through the MPL and the fibre substrate of the GDL. Reaching the flowfield channels, it is removed by the gas flow. Furthermore, normally a temperature gradient between reaction layer and flowfield exists. The relative humidity depends on the actual operating conditions, but generally a very high value near the reaction layer will decrease to the value imposed by the external humidification of the reactant gases in the channel region. Still, it is not possible to simulate gas flows within a grand canonical MC model, but steady-state conditions are feasible. By presetting the water partial pressure within the three-dimensional system, one is able to simulate regions and conditions within the GDL where phase transitions take place. After reaching a steady state, the resulting mean water distribution can be analysed and compared to experimental visualization data. For a more detailed description of the analysis of the mean water distribution see Section 5.3.

Water transport by the gas phase is not explicitly treated within the model. Assuming that the related water transport phenomena in the gas phase, i.e. removal of humidity from sites where evaporation takes place and delivering towards sites where condensation occurs, are not limiting under the steady-state operating conditions of the real cell, the relevant processes, i.e. movement of liquid water, condensation and evaporation according to the local relative humidity and temperature are described by the model. Of course, water transport within the flowfield channels of the operating cell is greatly influenced by the bulk gas flow, whereas within the GDL,

diffusion constitutes the main gas transport mechanism, and bulk flow velocities are by orders of magnitude lower than in the channel so they can be neglected in most cases. Thus, our model does not aim at describing the movement of water droplets within the flowfield channels, which would not be feasible employing the MC technique as used here. Instead, we strive towards describing the steady-state water distribution within the GDL substrate and the μm scale pores of the MPL. The model accounts for the solid flowfield ribs in a realistic way, while the free space of the channel rather serves as open boundary and the water distribution within this open space is not subject to further analysis. Cf. Section 5.3.5 for a detailed description of the cut-out of the cell used for the simulations.

The grand canonical approach is especially suitable for systems where one is interested in mean properties as a function of external conditions e.g. in adsorption studies [74]. In the case of a fuel cell these parameters are: temperature, relative humidity and of course the surface properties of the respective GDL and flowfield material (contact angle of water against the respective material corresponding to surface energy values).

5.1. Basic equations

For a grand canonical approach, Eq. (7) has to be complemented by two additional equations: the acceptance probabilities for particle insertion and removal. Following [74] we write:

$$a_{N \to N+1} = \min\left\{ 1, \frac{V}{\varLambda^3 (N+1)} \exp[\beta[\mu - U(N+1) + U(N)]] \right\}$$
(14)

$$a_{N \to N-1} = \min\left\{ 1, \frac{\varLambda^3 N}{V} \exp[-\beta[\mu + U(N-1) - U(N)]] \right\}$$
(15)

$\varLambda$ is called the thermal de Broglie wavelength.

5.2. Implementation within the μm-scale model

To obtain a grand canonical MC model working on the μm-scale, these equations have to be transformed. Hence, the calculation of the chemical potential has to be adapted for a simulation on the μm-scale. The chemical potentials for the liquid and gas phase can

be obtained from the usual thermodynamic expressions (see e.g. Ref. [79]):

$$\mu_{\text{fluid}} = \mu_0 - c_{p_{\text{fluid}}}\ln\left(\frac{T}{T_0}\right) + RT\ln\left(\frac{p_{\text{vap}}}{p_0}\right) \tag{16}$$

$$\mu_{\text{vap}} = \mu_0 - c_{p_{\text{vap}}}\ln\left(\frac{T}{T_0}\right) + RT\ln\left(\frac{p_{\text{partial}}}{p_0}\right) \tag{17}$$

μ_0: chemical potential under standard conditions
$c_{p_{\text{fluid}}}$: constant pressure thermal capacity of the fluid
$c_{p_{\text{vap}}}$: constant pressure thermal capacity of water vapour
p_0: 1013.25 hPa
T_0: 393 K
p_{vap}: water vapour pressure
p_{partial}: water partial pressure in the gas phase

As a special feature of our model, not only the chemical potentials are included, but also changes in surface energy occurring during evaporation/condensation are considered. Thus, we can rewrite Eqs. (14) and (15) as

$$a_{N\to N+1} = \min\left\{1, \exp\left[-\frac{\beta_2}{T}\left(\left(\mu_{\text{fluid}} - \mu_{\text{vap}}\right)\cdot n + \left(E_{\text{fluid}} - E_{\text{vap}}\right)\right)\right]\right\} \tag{18}$$

$$a_{N\to N-1} = \min\left\{1, \exp\left[-\frac{\beta_2}{T}\left(\left(\mu_{\text{vap}} - \mu_{\text{fluid}}\right)\cdot n + \left(E_{\text{vap}} - E_{\text{fluid}}\right)\right)\right]\right\} \tag{19}$$

where β_2 is defined as the geometric mean of the 'bulk' thermodynamic constant nR (n is the number of moles) and the 'surface' constant β_1:

$$\beta_2 = \frac{1}{\sqrt{N_S k_B \cdot nR}} \tag{20}$$

For the calculation of β_1 only the water molecules are considered which contribute to the surface energy. The definition of β_2 thus reflects that in the case of phase transition the chemical potential and the surface energies contribute to the acceptance probability.

Now, each MC iteration consists of one tentative movement per water voxel and one evaporation/condensation attempt per water and free voxel, respectively.

5.3. Steady-state simulations

5.3.1. Definition of a steady state

The objective of the MC simulations performed herein is to obtain information about the mean water distribution within the GDL substrate. Every thermodynamic system attempts to minimize the free energy, which means in the end that water will avoid hydrophobic surfaces by forming drops with only a small interface to this surface. During a MC simulation, often several hundred thousand MC iterations are necessary to reach such a steady state. Within the grand canonical MC model, a steady-state can be characterized by:

- Convergence of the number of water moves.
- Convergence of the number of condensation and evaporation events to the same value.
- Convergence of the mean water content.

5.3.2. Simulation parameters

Our MC model is working on a three-dimensional lattice with a voxel size of $5 \times 5 \times 5$ µm^3. To keep CPU times moderate, the maximum system size used within our grand canonical MC model is $500 \times 250 \times$ (GDL thickness + rib) µm^3. As will be detailed in the following, the GDL thickness is around 140 µm depending on whether the GDL is compressed by the flowfield ribs or not. Besides the surface energies of the respective materials, the boundary conditions (relative humidity, temperature, gradients) have to be preset especially for the grand canonical approach.

5.3.3. Analysis of the mean water distribution

To analyse the mean water distribution after reaching a steady state, additionally 0.5 million MC iterations were performed to obtain reliable average values. Afterwards, the water amount is averaged over these iterations. A voxel is identified as water-occupied voxel if it is allocated by water with a probability of 70%. Ultimately, the choice of this threshold value is to some extend arbitrary. Using some test cases, it was checked that the resulting mean water occupation was not very sensitive to the actual value chosen, although it is evident that when taking a lower threshold value, say 50%, one would obtain a larger average total amount of water. But as has been discussed in Ref. [41], if it is observed that an extended region of the system is covered by water in more than 70% of all steady-state configurations, one can be quite sure that this corresponds to a significant water agglomeration. In addition to the mean 3-D water distribution, also e.g. the mean water amount per z-layer can be calculated. Furthermore, we are able to separate the water of the channel region from the water under the ribs which helps to obtain the differences in the water distributions for these regions.

5.3.4. Simple systems

To demonstrate the ability of the model to correctly reproduce the properties of water in contact to a solid surface, the formation of drops of liquid water on different hydrophobic/hydrophilic surfaces was investigated. To connect the surface energy values to the internal contact angle, we use the Young equation in the following way:

$$\cos\theta = \frac{\Delta\gamma}{\gamma_{\text{lv}}} \tag{21}$$

by setting $\gamma_{\text{sl}} = 0$ we obtain $\Delta\gamma = \gamma_{\text{sv}}$.

This means that only the contact angle of water against the solid and the surface energy liquid/vapour ($\gamma_{\text{lv}} \approx 72,9$ N m^{-2} see e.g. literature [80,81]) are required to calculate the energy difference $\Delta\gamma$. This information then serves as input for the MC model.

In Fig. 2, exemplary results for simple systems with smooth surfaces featuring different contact angles are shown. The drop shapes resulting from the preset energy values are conform to the expectations based on the respective contact angle. Consequently, the wetting behaviour is described correctly within the canonical MC simulations.

To demonstrate the ability of the grand canonical MC model to simulate condensation and evaporation in a physically correct manner, simulations of a simple system at different external conditions were performed. The system was initialized half-filled with a smooth hydrophilic surface at the bottom (contact angle of 8° which equates to the contact angle of a glass surface according to Ref. [82]). Besides simulations at the equilibrium state (373.15 K and 1 bar), small temperature variations have been performed. The resulting mean water distributions are illustrated in Fig. 3. Reproducing the correct thermodynamic behaviour, if the temperature

deviates from the equilibrium state (373.15 K and 1 bar), the system gets filled or emptied.

5.3.5. Representation of the cathode GDL and flowfield

As has been described in the first publication concerning our MC model [41] in more detail, we are modelling the water distribution within the cathodic GDL. Because of computational limitations, we are not able to simulate the water distribution for the whole cell area. Our extract consists of a section of the cathodic GDL and the flowfield channel and rib above it, but the latter do not extend to full depth. In the following, the x- and y-directions lie within the plane of the GDL, while the positive z-axis denotes the direction from the reaction layer towards the flowfield. Hereby, the x-direction points orthogonal to, the y-axis along the flowfield channel.

6. Results

6.1. Experimental results

6.1.1. Surface energy and contact angle

The results obtained for the 25 BC GDL material can be found in Table 2. Unfortunately, the value of 92° for the contact angle to water cannot be directly compared to a value from literature for the same material. Nevertheless, some values to compare are available, Wood et al. [7] report 99.2° for a SGL GDL 24 BC obtained by extrapolation from their Owens–Wendt analysis, 100.8° for a GDL 24 BA, for a 10 BC they find 99.7° and 101.2° in the case of 10 BA. All of these are manufactured by SGL, and the weight ratio of PTFE is used is publicly available, BC means 5 wt% in the GDL substrate and 23 wt% in the MPL, BA 5 wt% in the substrate and no MPL. For the 24 BA material, Wood et al. also performed a single-fibre Wilhelmy measurement giving a contact angle of approx. 82° (assessed from Fig. 10 in lit. [7]), so, as already mentioned, they find a difference of about 19° by which the single-fibre measurement gives a lower contact angle. As discussed above, the IGC method is expected to give results comparable to the single fibre Wilhelmy method, because both measure the real inner-surface property without being influenced by structural properties of the material. The value found here lies below the Owens–Wendt values reported by Wood et al., as would be expected, and within a realistic bandwidth. The single-fibre BA material investigated by Wood et al. features even lower values, but as mentioned, it cannot be directly compared, apart from the fact that these GDLs lack a MPL, also e.g. the graphitization procedures are not published. Parry et al. [14] report 90° ± 3 at 20 °C from an Owens–Wendt extrapolation and 89° for a direct Washburn measurement with water at 66 °C for the GDL that they call P5, which also has 5 wt% PTFE in the substrate and an (unspecified) MPL. These values are in very good agreement to our result, but of course it is difficult to compare material we do not know more about.

It is worth noting that the contact angle obtained here is an integral value giving an overall representation of the GDL including the MPL and the substrate. The same holds true for the Owens–Wendt values mentioned above, which are based on liquid sorption measurements. Comparing the contact angles obtained by Wood et al. [7] for a SGL GDL 24 BC (with MPL, 99.2°) and for a GDL 24 BA (same substrate without MPL, 100.8°) as already mentioned above, one can assess that the addition of an MPL does not crucially influence the overall wetting properties. But obviously, from the point of view of modelling the wetting properties of the GDL on the μm-scale, it would be beneficial to obtain the corresponding, locally resolved data. To the best of our knowledge, this is currently not feasible. To get, at least, an idea whether the effect of local differences in wettability would be crucial for the results of the simulation, we decided to compare the results of the model for two

cases, a uniform contact angle all over the GDL and a random distribution of hydrophobic and hydrophilic spots resulting in the same overall properties as measured in experiment, cf. Section 6.2.

The reason for choosing the GDL 25 BC for this study was that the result should serve as simulation input for the MC study and at the same time, this GDL was used for the synchrotron in-situ experiments. Clearly, it would be desirable to obtain values directly comparable to literature, so both the Owens–Wendt method for the 25 BC and IGC measurements for GDLs which can be better compared to the literature values should be performed. First results of additional materials will be reported in a subsequent publication.

6.1.2. Visualization of water in an operated fuel cell

The tomography measurements reveal the structural information of the fuel cell in dry and operated state. As explained in Section 2.2, the information of the water distribution can be extracted from this data. Thus, by combining the information of the water distribution and the dry cell, a differentiation between water and the carbon fibre substrate in the tomogram is achieved. This is illustrated for the complete tomogram of the fuel cell in Fig. 4. At the operating conditions chosen (see Table 3), liquid water is forming in the channel as well as within the GDL. In Fig. 4(b), the water appears not equally distributed, instead a difference between the area of the channel and the land can be observed. For a deeper analysis, the water amount along the z-axis is calculated for each layer and differentiated between channel and land area. To obtain a realistic representation of the water distribution, regions with artefacts (along the tomogram axis) and regions influenced by the channel turns are left out. In total 12 regions in the channel area and 10 regions under the land, each having an area of $2200 \times 400 \ \mu m^2$, were analysed (Fig. 5). The mean value of the water amount per area in each layer was calculated. As a result, the average water distribution for channel and land area can be compared along the z-axis as shown in the diagram (Fig. 6). This separation in land and channel region can also be performed for the simulation results which enables a direct comparison of both the experimental and modelling results. A maximum in the water distribution is found for the land region at $z = 100 \ \mu m$ which is right below the land ($z = 120 \ \mu m$). Water which is produced in the electrochemically active area under the land faces a longer transport path through the GDL. Furthermore, the gas flow is especially low right below the ribs, so water tends to accumulate there. Thus, the highest water accumulation in Fig. 6 is found for the land area in this layer.

In contrast, the maximum in the channel region is shifted. Due to the open space of the gas channel, water can accumulate on the GDL surface before it is discharged by the gas flow. Consequently, the highest water density is found at the interface of GDL and channel ($z = 130 \ \mu m$). A second peak is found at $z = 50 \ \mu m$ which is close to the interface of GDL and MPL. Water which was produced within the reaction layer, then has been transported through the micro porous layer, is now accumulating in the more macro porous substrate near the MPL before it is discharged towards the channel. This characteristic is less pronounced for the land region, here only an inflection point is found at $z = 40 \ \mu m$. For comparison with the Monte Carlo simulation results, appropriate cutouts of a part of the tomogram have been chosen. This part is illustrated in dry and operated state in Figs. 7 and 8, which shows the top view of this extract in which the regions used as input for the Monte Carlo model are marked. Each cutout has a size of $240 \times 240 \ \mu m^2$ and consists of one half which is compressed by the flowfield land and another half which is the region under the channel. The 3D visualization including the water distribution within these cutouts is shown in Fig. 9. The corresponding water distributions can be directly compared to the mean water distributions obtained by the

grand canonical MC simulations. This comparison will be presented in Section 6.2.

6.2. Simulation results

The grand canonical MC simulations were performed on the cutouts of the tomography data described in Section 6.1, i.e. the tomography images of the dry cell were used as model input. The size (240×240 μm^2) of these cutouts was chosen to meet the computational limitations of the model; using several regions (see also Fig. 8) enables us to obtain averaged results which should be at least semi-quantitatively comparable to the results obtained over a large part of the cathode area in experiment. Furthermore, they can be directly compared to the experimental result for the respective cutout. Only the structural information of the GDL was directly used as model input. The flowfield ribs were artificially generated to allow for assigning different material properties (contact angle against water) for this kind of material. Furthermore, using a simple rib structure facilitated the separation of the rib and the channel region from each other because the dimension of the rib/channel region was the same for every cutout. As a further restriction due to the computational limitations, the rib depth is also smaller then in the real flowfield. Unfortunately, using an artificial rib structure involves losing the information about the material roughness of the flowfield which is clearly visible from Fig. 9. The experimental flowfield is milled which explains the roughness.

As our model uses periodic boundary conditions in *x*- and *y*-direction, it only makes sense to use a system covering a whole rib-channel-rib unit in *x*-direction. Consequently, the data obtained from the cutouts has to be mirrored parallel to the *y*-axes before it can serve as model input. The dimensions of the cutouts in Fig. 8 is $240 \times 240 \times 245$ μm^3 resulting in $480 \times 240 \times 245$ μm^3 after mirroring. Without such mirroring, one would find compressed GDL data on the one edge (position $x = 0$, GDL material under rib) and less compressed material at the other edge ($x = 49$, GDL material under channel) in direct neighbourhood due to the periodic boundary conditions which would not make any sense.

In Table 4 the simulation parameters are summarized. Two different MC studies were performed using the same external conditions (temperature and relative humidity), but two different realizations of the wetting properties obtained from experiment. In study 1, a mixed wettability of the material on the μm scale is presumed, i.e. a random mixture of hydrophobic and hydrophilic surface regions yielding the wetting properties which were observed on the macroscopic level. Employing such a mixed wettability seems appropriate because the PTFE coverage of the fibres in reality can be expected to be non-uniform as well. To implement this in the model, two types of surface are randomly distributed in a ratio such that the resulting surface energy corresponds to the value measured. The surface properties are constituted by setting appropriate values for $\Delta\gamma$ in Eq. (21) and determining their ratio according to

$$-12.7x + 41.8y = -2.89$$

$$x + y = 1$$

$$\Rightarrow x = 0.82; \quad y = 0.18$$

This means that 82% of the GDL surface is covered by hydrophobic material and 18% by material which shows hydrophilic wetting behaviour. Within the MC model, the hydrophobic material is randomly distributed over the originally hydrophilic GDL material until the preset percentage is reached. In study 2, a uniform wettability corresponding to a contact angle of 92 °against water is

employed. In contrast to the non-uniform surface mentioned above, this directly reflects the integral wetting properties measured, thereby assuming that any inhomogeneity − which may still be possible on the sub-μm-scale − is not relevant on the scale reflected by the model.

Fig. 10 shows the resulting mean water distribution for two of the cutouts, respectively, for GDL material featuring a contact angle distribution and a uniform contact angle. Visually, one can only identify some small differences in the mean water distribution comparing the results for the contact angle distribution and the uniform contact angle for the same cutout. The mean water distribution of two different cutouts show more severe differences even though the water agglomerations can be found in principle at the same locations for both cutouts: large water clusters under and on the ribs and smaller agglomerations within the GDL pores. Furthermore, this also demonstrates why it is necessary to average over several cutouts to obtain representative data which can be compare to experiment. The water agglomerations within the porous material differ due to the varying pore structure from cutout to cutout.

6.3. Comparison of the simulation results to the experimental data

To compare the water amount within the GDL for the MC simulations to the experimental visualization data, an analysis of the water distribution of the same cutouts was performed for both the experimental and the modelling results. Averaging the mean water amount per z-layer over these cutouts facilitates a direct comparison for the total water amount as well as for the channel and the rib regions. The results from experiment are presented in Fig. 11, the results for the simulations in Fig. 12. Regarding the locations of the locations of the maxima, the curve shapes are in good agreement. The experimental data has the first maximum at $z \approx 50$ μm, i.e. within the GDL, and a second peak rising from ≈ 110 μm regarding the curve for the total water amount. For the simulations, one obtains similar curve shapes with a first maximum at $z \approx 50$ μm (both for uniform contact angle and contact angle distribution). The second maximum is located at ≈ 120 μm for both simulation studies. Regarding the water amount per z-layer divided according to channel and rib regions, the curve shapes for the channel are quite similar for both the experiment and the simulations. In the case of the rib region, one can identify the influence of the flowfield roughness within the curve shape of the experimental data. Here, the water amount is decreasing slowly from the position of the rib edge on ($z \approx 135$ μm), while it is immediately going to zero for the MC simulations. By trend, the absolute values for the modelling results observed here are lower than the experimental values. This may be due to the fact that the total content is quite sensitive to the value of the relative humidity preset for the simulations, whereas the experimental humidity value contains significant uncertainty. Overall, the differences between the study employing a uniform surface model and the one featuring an inhomogeneous distribution of wettability are rather minor and the basic results that can be concluded are equivalent, although the curves do not fit exactly.

7. Conclusions

To achieve realistic simulation results of water within fuel cell GDLs on the μm-scale, the model applied has to be able to reproduce the behaviour of liquid water in contact with the GDL structure and furthermore, it should be able to simulate evaporation and condensation under boundary conditions based on actual operating conditions of the cell. Hence, we extended the MC model presented in Ref. [41], which was primarily focused on ageing phenomena then, in terms of an improved description of the liquid−solid phase

boundaries and by the inclusion of phase transitions. As an essential prerequisite of a physically correct description of the solid—liquid interactions, the wetting properties on the inner surface of the porous material must be known. To verify the simulation results on a firm experimental basis, one has to be able to detect the water distribution within the GDL on the length scale of the underlying porous structure, i.e. with a resolution of a few µm in the case of the GDL substrate.

Approaching this challenge in a threefold way, we have been further developing the MC model to amend and improve its simulation capability accordingly. Considering simple systems the physics of which is easy to understand, we successfully demonstrated that the model is capable of describing the phenomena required. Furthermore, by performing surface energy measurements applying the sophisticated inverse gas chromatography method, we were able to gain the input parameters necessary to describe the surface interactions relevant on this scale. Finally, a setup including advanced synchrotron tomography techniques and a special cell design allowed for obtaining reliable experimental reference data in high resolution.

Taking the dry structure obtained from tomography and the surface properties measured as input for the simulations, water agglomerations within several cutouts of the structure could be investigated and averaged giving an integral picture of the water distribution within the GDL. Comparing the simulation results to the experimental water distribution yielded a very good qualitative agreement of the amount of water found and an even quantitative compliance of the positions of the maxima found. In accordance, both imaging and simulation results show that the GDL region just below the flowfield ribs is especially prone to the accumulation of liquid water, whereas below the channel, a second maximum corresponding to the interface of MPL and fibre substrate appears more pronounced than below the ribs.

Thus, grand canonical MC modelling of the fuel cell GDL constitutes a powerful tool for predicting and explaining the behaviour of liquid water within the GDL substrate under steady state conditions rendering e.g. the investigation of ageing effects or testing of structure modifications possible. Synchrotron tomography provides a unique tool to make the processes involving liquid water within a fuel cell under operation accessible to investigation.

Acknowledgement

References

[1] A. Arvay, E. Yli-Rantala, C.-H. Liu, X.-H. Peng, P. Koski, L. Cindrella, P. Kauranen, P. Wilde, A. Kannan, Journal of Power Sources 213 (2012) 317—337.
[2] J.T. Gostick, M.A. Ioannidis, M.W. Fowler, M.D. Pritzker, Journal of Power Sources 194 (2009) 433—444. XIth Polish Conference on Fast Ionic Conductors 2008.
[3] P. Krüger, H. Markötter, J. Haußmann, M. Klages, T. Arlt, J. Banhart, C. Hartnig, I. Manke, J. Scholta, Journal of Power Sources 196 (2011) 5250—5255.
[4] H. Markötter, I. Manke, P. Krüger, T. Arlt, J. Haußmann, M. Klages, H. Riesemeier, C. Hartnig, J. Scholta, J. Banhart, Electrochemistry Communications 13 (2011) 1001—1004.
[5] H. Markötter, I. Manke, J. Haußmann, T. Arlt, M. Klages, P. Krüger, C. Hartnig, J. Scholta, B. Müller, H. Riesemeier, J. Banhart, Micro & Nano Letters, IET 7 (2012) 689—692.
[6] V. Gurau, M.J. Bluemle, E.S. De Castro, Y.-M. Tsou, J.A. Mann Jr., T.A. Zawodzinski Jr., Journal of Power Sources 160 (2006) 1156—1162. Special issue including selected papers presented at the International Workshop on Molten Carbonate Fuel Cells and Related Science and Technology 2005 together with regular papers.
[7] D.L. Wood, C. Rulison, R.L. Borup, Journal of The Electrochemical Society 157 (2010) B195—B206.
[8] J.Z. Fishman, H. Leung, A. Bazylak, International Journal of Hydrogen Energy 35 (2010) 9144—9150. The 1st Iranian Conference On Hydrogen & Fuel Cell.
[9] A.B.D. Cassie, S. Baxter, Transactions of Faraday Society 40 (1944) 546—551.
[10] A.B.D. Cassie, Discussions of the Faraday Society 3 (1948) 11—16.
[11] J. Gostick, M. Fowler, M. Ioannidis, M. Pritzker, Y. Volfkovich, A. Sakars, Journal of Power Sources 156 (2006) 375—387.
[12] E.W. Washburn, Physical Review 17 (1921) 273—283.
[13] D. Owens, R. Wendt, Journal of Applied Polymer Science 13 (1969) 1741—1747.
[14] V. Parry, E. Appert, J.-C. Joud, Applied Surface Science 256 (2010) 2474—2478.
[15] G. Chen, H. Zhang, H. Ma, H. Zhong, International Journal of Hydrogen Energy 34 (2009) 8185—8192.
[16] F. Thielmann, Journal of Chromatography A 1037 (2004) 115—123. Estimation of Physicochemical Properties by Chromatographic and Electrophoretic Techniques.
[17] M.D. Jones, P. Young, D. Traini, Advanced Drug Delivery Reviews 64 (2012) 285—293. Lactose as a carrier for inhalation products.
[18] C. Van Oss, R. Good, M. Chaudhury, Langmuir 4 (1988) 884—891.
[19] C. Della Volpe, S. Siboni, Journal of Colloid and Interface Science 195 (1997) 121—136.
[20] C. Della Volpe, D. Maniglio, S. Siboni, M. Morra, Journal of Adhesion Science and Technology 17 (2003) 1477—1505.
[21] A.M. Kannan, L. Munukutla, Journal of Power Sources 167 (2007) 330—335.
[22] P. Nguyen, T. Berning, N. Djilali, Journal of Power Sources 130 (2004) 149—157.
[23] Z. Wang, C. Wang, K. Chen, Journal of Power Sources 94 (2001) 40—50.
[24] D. Wolf-Gladrow, Lattice-gas Cellular Automata and Lattice Boltzmann Models: An Introduction, Springer Verlag, Berlin Heidelberg New York, 2000.
[25] I. Fatt, Transactions of AIME 207 (1956) 144—181.
[26] S.P. Kuttanikkad, M. Prat, J. Pauchet, Journal of Power Sources 196 (2011) 1145—1155.
[27] J. Gostick, M. Ioannidis, M. Fowler, M. Pritzker, Journal of Power Sources 173 (2007) 277—290.
[28] M. Allen, D. Tildesley, Computer Simulation of Liquids, Oxford University Press, Oxford, 1990.
[29] D. Frenkel, B. Smit, Understanding Molecular Simulation: From Algorithms to Applications, Academic Press, 2002.
[30] D. Rapaport, The Art of Molecular Dynamics Simulation, second ed., Cambridge University Press, 2004.
[31] J. Haile, Molecular Dynamics Simulation: Elementary Methods, John Wiley & Sons, Inc., New York, NY, USA, 1992.
[32] N. Metropolis, A. Rosenbluth, M. Rosenbluth, A. Teller, E. Teller, The Journal of Chemical Physics 21 (1953) 1087—1092.
[33] R. Paul, H. Rieger, The Journal of Chemical Physics 123 (2005) 024708.
[34] M. Hashemi, M. Sahimi, B. Dabir, Physica A 267 (1999) 1—33.
[35] S. Jain, M. Acharya, S. Gupta, A. Bhaskarwar, Computers & Chemical Engineering 27 (2003) 385—400.
[36] J. Zalc, S. Reyes, E. Iglesia, Chemical Engineering Science 58 (2003) 4605—4617.
[37] J. Abel, A.A. Kornyshev, W. Lehnert, Journal of The Electrochemical Society 144 (1997) 4253—4259.
[38] M. Van Doormaal, J. Pharoah, International Journal for Numerical Methods in Fluids 59 (2008) 75—89.
[39] M. Tomadakis, S. Sotirchos, AIChE Journal 37 (2004) 74—86.
[40] F. Transvalidou, S. Sotirchos, AIChE Journal 42 (2004) 2426—2438.
[41] K. Seidenberger, F. Wilhelm, T. Schmitt, W. Lehnert, J. Scholta, Journal of Power Sources 196 (2011) 5317—5324.
[42] K. Seidenberger, M. Klages, F. Wilhelm, J. Scholta, ECS Transactions 42 (2012) 179—190.
[43] A. Singh, J. Lu, R. Aga, B. Yakobson, The Journal of Physical Chemistry C 115 (2011) 2476—2482.
[44] M. Szöri, M. Roeselova, P. Jedlovszky, The Journal of Physical Chemistry C 115 (2011) 19165—19177.
[45] M. Eikerling, Journal of The Electrochemical Society 153 (2006) E58—E70.
[46] Y. Wang, K. Chen, Journal of The Electrochemical Society 158 (2011) B1292.
[47] K. Loo, K. Wong, Y. Lai, S. Tan, C. Tse, IEEE Transactions on Energy Conversion (2011) 1—11.
[48] S. Strahl, A. Husar, M. Serra, Journal of Power Sources 196 (2011) 4251—4263.
[49] Y.B. Salah, Y. Tabe, T. Chikahisa, Journal of Power Sources 199 (2012) 85—93.
[50] J. Becker, C. Wieser, S. Fell, K. Steiner, International Journal of Heat and Mass Transfer 54 (2011) 1360—1368.
[51] S. Kandlikar, Z. Lu, T. Lin, D. Cooke, M. Daino, Journal of Power Sources 194 (2009) 328—337.
[52] C. Hartnig, I. Manke, R. Kuhn, S. Kleinau, J. Goebbels, J. Banhart, Journal of Power Sources 188 (2009) 468—474.
[53] I. Manke, C. Hartnig, N. Kardjilov, H. Riesemeier, J. Goebbels, R. Kuhn, P. Krüger, J. Banhart, Fuel Cells 10 (2010) 26—34.
[54] R. Kuhn, J. Scholta, P. Krüger, C. Hartnig, W. Lehnert, T. Arlt, I. Manke, Journal of Power Sources 196 (2011) 5231—5239.
[55] N. Kardjilov, I. Manke, A. Hilger, M. Strobl, J. Banhart, Materials Today 14 (2011) 248—256.

[56] C. Hartnig, I. Manke, N. Kardjilov, A. Hilger, M. Grünerbel, J. Kaczerowski, J. Banhart, W. Lehnert, Journal of Power Sources 176 (2008) 452–459.

[57] I. Manke, C. Hartnig, N. Kardjilov, M. Messerschmidt, A. Hilger, M. Strobl, W. Lehnert, J. Banhart, Applied Physics Letters 92 (2008). 244101–244101-3.

[58] I. Manke, C. Hartnig, M. Grünerbel, J. Kaczerowski, W. Lehnert, N. Kardjilov, A. Hilger, J. Banhart, W. Treimer, M. Strobl, Applied Physics Letters 90 (2007) 184101.

[59] J. Eller, T. Rosén, F. Marone, M. Stampanoni, A. Wokaun, F. Büchi, Journal of The Electrochemical Society 158 (2011) B963–B970.

[60] M. Khandelwal, S. Lee, M.M. Mench, Journal of The Electrochemical Society 156 (2009) B703–B715.

[61] M. Khandelwal, M. Mench, Journal of Power Sources 195 (2010) 6549–6558.

[62] H. Markötter, I. Manke, R. Kuhn, T. Arlt, N. Kardjilov, M.P. Hentschel, A. Kupsch, A. Lange, C. Hartnig, J. Scholta, J. Banhart, Journal of Power Sources 219 (2012) 120–125.

[63] W. Görner, M. Hentschel, B. Müller, H. Riesemeier, M. Krumrey, G. Ulm, W. Diete, U. Klein, R. Frahm, Nuclear Instruments and Methods in Physics Research Section A: Accelerators, Spectrometers, Detectors and Associated Equipment 467 (2001) 703–706.

[64] J. Banhart, A. Borbely, K. Dzieciol, F. Garcia-Moreno, I. Manke, N. Kardjilov, A. Kaysser-Pyzalla, M. Strobl, W. Treimer, International Journal of Materials Research 101 (2010) 1069–1079.

[65] S. Williams, A. Hilger, N. Kardjilov, I. Manke, M. Strobl, P. Douissard, T. Martin, H. Riesemeier, J. Banhart, Journal of Instrumentation 7 (2012) P02014.

[66] I. Manke, H. Markötter, C. Tötzke, N. Kardjilov, R. Grothausmann, M. Dawson, C. Hartnig, S. Haas, D. Thomas, A. Hoell, C. Genzel, J. Banhart, Advanced Engineering Materials 13 (2011) 712–729.

[67] J. Raula, F. Thielmann, M. Naderi, V.-P. Lehto, E.I. Kauppinen, International Journal of Pharmaceutics 385 (2010) 79–85.

[68] P. Uhlmann, S. Schneider, Journal of Chromatography A 969 (2002) 73–80. First International Conference on Inverse Gas Chromatography.

[69] M. Rückriem, A. Inayat, D. Enke, R. Gläser, W.-D. Einicke, R. Rockmann, Colloids and Surfaces A: Physicochemical and Engineering Aspects 357 (2010) 21–26. Characterization of Porous Materials: From Angstroms to Millimeters. A Collection of Selected Papers presented at the Fifth International Workshop CPM-5.

[70] P.P. Ylä-Mäihäniemi, J.Y.Y. Heng, F. Thielmann, D.R. Williams, Langmuir 24 (2008) 9551–9557.

[71] R.J. Good, Journal of Adhesion Science and Technology 6 (1992) 1269–1302.

[72] G.M. Dorris, D.G. Gray, Journal of Colloid and Interface Science 77 (1980) 353–362.

[73] S. Dong, M. Brendl, J. Donnet, Chromatographia 28 (1989) 469–472.

[74] D. Frenkel, in: N. Attig (Ed.), Computational Soft Matter: From Synthetic Polymers to Proteins, NIC Series, vol. 23, John von Neumann Institute for Computing, Jülich, 2004, pp. 29–60.

[75] E. Raymond, T. Tarbuck, M. Brown, G. Richmond, The Journal of Physical Chemistry B 107 (2003) 546–556.

[76] B. Garrett, G. Schenter, A. Morita, Chemical Reviews 106 (2006) 1355–1374.

[77] A. Braslau, M. Deutsch, P. Pershan, A. Weiss, J. Als-Nielsen, J. Bohr, Physical Review Letters 54 (1985) 114–117.

[78] H. Kuchling, Taschenbuch der Physik, Fachbuchverlag, Leipzig, 2001.

[79] G. Wedler, Lehrbuch der Physikalischen Chemie, fifth ed., WILEY-VCH, Weinheim, 2004.

[80] C. Van Oss, R. Good, Journal of Macromolecular Science Chemistry 26 (1989) 1183–1203.

[81] R.C. Weast (Ed.), CRC Handbook of Chemistry and Physics, 65th ed., CRC Press, Inc., Boca Raton, Florida, 1984.

[82] P. von Böckh, Fluidmechanik: Einführendes Lehrbuch, second ed., Springer-Lehrbuch, Springer-Verlag, Berlin Heidelberg New York, 2004.